EXACT RESULTS OF THE VECTOR THEORY OF COHERENT BACKSCATTERING FROM DISCRETE RANDOM MEDIA: AN OVERVIEW

MICHAEL MISHCHENKO,[1] VICTOR TISHKOVETS,[2] AND PAVEL LITVINOV[3]
[1]*NASA Goddard Institute for Space Studies, 2880 Broadway, New York, NY 10025, USA*
[2]*Kharkiv Astronomical Observatory, 35 Sumskaya St., 61022 Kharkiv, Ukraine*
[3]*Institute of Radioastronomy of NASU, 4 Chervonopraporna St., Kharkiv, Ukraine*

Abstract. Coherent backscattering of light by discrete random media, otherwise known as weak photon localization, is a remarkable optical phenomenon caused by constructive interference of waves propagating along the same light-scattering paths but in opposite directions. A well-known manifestation of coherent backscattering is an intensity peak centered at exactly the backscattering direction. It also has been established that when the incident beam is unpolarized then the coherent backscattering intensity peak can be accompanied by a sharp asymmetric peak of negative polarization with a minimum centered at a very small phase angle. It has been suggested that coherent backscattering could be a contributor to some effects observed for solar system bodies in visible light and at radiowave frequencies [1–4]. However, accurate theoretical computations of weak photon localization based on first physical principles are difficult and have been used in analyses of planetary observations in only a handful of publications. This chapter briefly discusses manifestations of coherent backscattering and reviews the exact theory of this phenomenon and its applications to analyses of laboratory data and remote-sensing observations.

1. Introduction

It has been realized recently that diffuse, incoherent multiple scattering of electromagnetic waves by media composed of randomly positioned, discrete scattering particles is always accompanied by a phenomenon called coherent

In G. Videen and M. Kocifaj (eds.), *Optics of Cosmic Dust*
(Kluwer Academic Publishers, Dordrecht, 2002), pp. 239-260

backscattering (or weak photon localization). This phenomenon has been actively studied over the last two decades both experimentally and theoretically [5–8]. Furthermore, by comparing observational data with theoretical computations, it has been shown that coherent backscattering of sunlight by regolithic grains can be responsible for two spectacular natural phenomena exhibited by Saturn's rings and some bright atmosphereless solar system bodies, viz., the spike-like photometric and sharp, asymmetric polarization opposition effects [9–11]. It also has been suggested that diffuse and coherent backscattering of electromagnetic waves might explain unusual radar returns for icy outer planet satellites, polar caps on Mars and Mercury, and some terrestrial lava flows [3,12–16]. In this case, multiple scattering can be caused by discrete scatterers in a relatively transparent matrix, e.g., by particulate rock and/or ice surfaces in air or rocks and voids imbedded in ice.

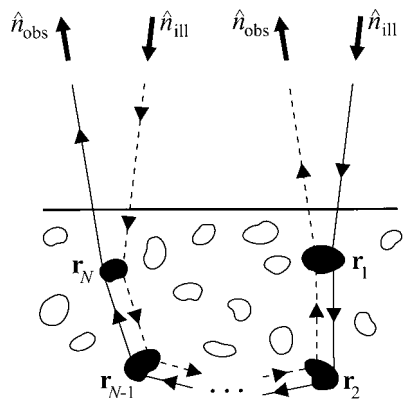

Figure 1: Schematic explanation of coherent backscattering.

To understand the physical origin of weak photon localization, let us consider a layer composed of discrete, randomly positioned scattering particles and illuminated by a parallel beam of light incident in the direction $\hat{n}_{\rm ill}$ (Fig. 1). A distant observer measures the intensity of light reflected by the layer in the direction $\hat{n}_{\rm obs}$. The reflected signal is a result of the contributions from waves scattered along various paths inside the layer involving different combinations of particles. Let us consider two conjugate scattering paths shown in Fig. 1 by solid and dashed lines. These paths go through the same group of N particles, denoted by their positions $\mathbf{r}_1$, $\mathbf{r}_2$,…, $\mathbf{r}_N$, but in opposite directions. The waves scattered along the two conjugate paths interfere, the interference being constructive or destructive depending on the phase difference $k(\mathbf{r}_N - \mathbf{r}_1)(\hat{n}_{\rm ill} + \hat{n}_{\rm obs})$, where $k = 2\pi/\lambda$ is the wave number and λ is the wavelength in the surrounding medium. If the observation direction is far from the exact backscattering direction given by $-\hat{n}_{\rm ill}$, then the waves

scattered along conjugate paths involving different groups of particles interfere in different ways, and the average effect of the interference is zero due to the randomness of particle positions. Consequently, the distant observer measures some average, incoherent intensity well described by the classical radiative transfer theory. However, at exactly the backscattering direction ($\hat{n}_{\text{obs}} = -\hat{n}_{\text{ill}}$), the phase difference between conjugate paths involving any group of particles is identically equal to zero and the interference is always constructive, thereby causing a coherent backscattering intensity peak.

Owing to its fundamental interference nature, coherent backscattering is a universal physical phenomenon, accompanies any multiple-scattering process, and occurs for particles of any size, shape, and refractive index. The angular width of the backscattering intensity peak can be very small for particles much smaller or much larger than the wavelength of the incident radiation [17], thereby often making the peak unobservable in passive remote sensing measurements. However, coherent backscattering almost always affects active observations with monostatic lidars and radars, e.g., radar observations of terrestrial and planetary surfaces.

Exact computations of the coherent backscattering effect based on solving the Maxwell equations are feasible only for few-particle clusters and is complicated by several factors. First, the scattering pattern for a monodisperse cluster of spheres in a fixed orientation is always heavily burdened by multiple interference maxima and minima and by an intricate resonance structure typical of single monodisperse spheres [18]. Second, the scattering pattern is further influenced by near-field effects, which result from component spheres in a closely packed cluster not being in the far-field zones of each other and can significantly suppress the coherent backscattering effect [19–21]. Third, simple trigonometry shows that the angular width of the coherent backscattering intensity peak is of the order of $1/k\langle d\rangle$, where $\langle d\rangle$ is the average distance between the cluster components. Therefore, this peak can be too broad to be reliably identified unless the cluster components are separated widely enough. However, increasing the distance between the cluster components diminishes the contribution of multiple scattering and, thus, the amplitude of the coherent backscattering peak, thereby making it difficult to detect. To smooth out the effect of the first factor and make the backscattering peak detectable, the scattering pattern must be averaged over particle sizes, cluster orientations, and distances between the components. Furthermore, the average distance between the cluster components must be much larger than the size of the components and the wavelength, but yet small enough so that the multiple-scattering contribution to the total signal remains significant.

The simplest case of two widely separated spheres with diameters much smaller than the wavelength was studied analytically in [22], but it was found that the amplitude of the coherent backscattering intensity peak was extremely

small because of the weakness of the multiple-scattering contribution to the total scattered signal. Mishchenko [23] applied the exact superposition *T*-matrix method [18] to polydisperse, randomly oriented clusters composed of two equal wavelength-sized spheres. He computed the ratio of intensities scattered by the clusters and by two independent spheres of the same size assuming that the incident light was unpolarized. Figure 2 shows this ratio versus scattering angle (i.e., the angle between the incident and scattered beams) calculated for $k\langle d\rangle = 25$. The average component sphere size parameter is $k\langle a\rangle = 5$, where a is the sphere radius, and the relative refractive index is $m = 1.2$. The curve clearly shows an enhancement of intensity with an angular width comparable to $1/k\langle d\rangle$ and an amplitude of about 1.03. This feature persisted with varying $k\langle d\rangle$, $k\langle a\rangle$, and refractive index, thereby indicating that it was indeed caused by coherent backscattering.

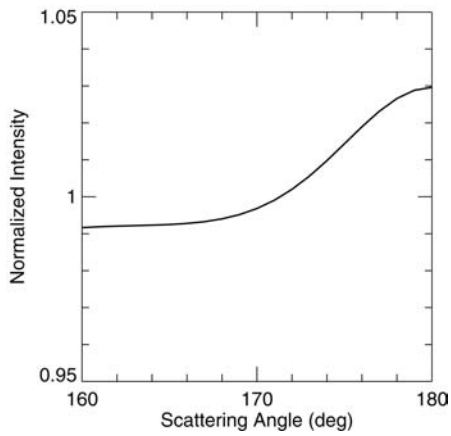

Figure 2: Coherent backscattering by polydisperse, randomly oriented two-sphere clusters.

The amplitude of the coherent backscattering peak can be significantly greater for scattering media composed of very large collections of particles (see Fig. 3 adapted from [24]). However, because of complicated multiple-scattering processes involved, exact physically-based computations of weak localization for such media are difficult and must often rely on one or more simplifying assumptions or must be replaced by approximate computations. The conventional theoretical tool for computing coherent backscattering has been the diffusion approximation [25,26]. However, although this approximation rather accurately predicts the angular profile of the backscattering intensity peak, it ignores the first-order-scattering contribution to the reflected light and, thus, cannot be used to compute the amplitude of the peak, i.e., the ratio of the intensity at the center of the peak to the incoherent background intensity. Furthermore, in

some cases the main physical characteristics of a particulate medium (e.g., particle size, shape, and refractive index) cease to be explicit model parameters [27], thereby making difficult, if even possible, comparisons of model computations with results of controlled laboratory experiments. An additional complexifying factor is that accurate computations of the amplitude and polarization state of the backscattering peak must explicitly take into account the vector nature of light since polarization effects have been shown to be extremely important in coherent backscattering [7,11,28–32]. Another theoretical approach is based on Monte-Carlo computations of multiple scattering that keep track of the phase relations between the scattered waves [33–35; see also the chapter by Muinonen *et al.*]. However, such computations are time-consuming and must be extensively tested versus exact theoretical results.

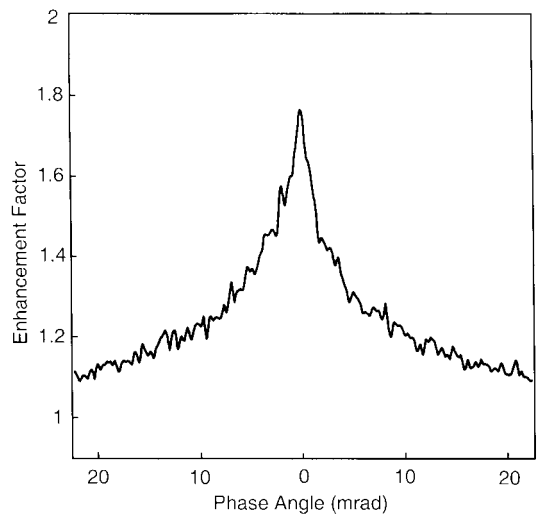

Figure 3: Angular profile of the coherent backscattering peak produced by a 1500-μm-thick slab of 9.6 vol% of 0.215-μm-diameter polystyrene spheres suspended in water. The slab was illuminated by a linearly polarized laser beam ($\lambda = 633\,\text{nm}$) incident perpendicularly to the slab surface. The scattering plane (i.e., the plane through the vectors $\hat{n}_{\text{ill}}$ and $\hat{n}_{\text{obs}}$) was fixed such that the electric vector of the incident beam vibrated in this plane. The detector measured the component of the backscattered intensity polarized parallel to the scattering plane. The curve shows the profile of the backscattered intensity normalized by the intensity of the incoherent background as a function of the phase angle α. The latter is defined as the angle between the vectors $\hat{n}_{\text{obs}}$ and $-\hat{n}_{\text{ill}}$.

In this chapter we review the exact theory of coherent backscattering for sparse discrete random media in which every scatterer is in the far-field zone of all other scatterers and the near-field effects can be neglected. The critical

advantages of this theory are that polarization effects are fully taken into account and that particle size distribution, shape, refractive index, and number density are explicit model parameters, thereby facilitating comparisons of theoretical and experimental results. In the following section we will discuss the characteristics of weak photon localization at the exact backscattering direction, in which case it is possible to derive a simple relationship between the diffuse and coherent contributions to the total Stokes reflection matrix applicable to particles of any size, shape, and refractive index. In sections 3 and 4 we will consider the angular dependence of coherent backscattering in the case of normal incidence of light on a plane-parallel slab composed of discrete scattering particles. We will also mention, where appropriate, the relevance of theoretical calculations to specific manifestations of coherent backscattering observed in laboratory and remote-sensing measurements.

2. Exact backscattering direction

Consider a plane-parallel layer composed of discrete, randomly and sparsely positioned particles. Let the medium be illuminated by a parallel beam of quasi-monochromatic radiation incident in the direction $\hat{n}_{\rm ill}$ and characterized by the four-component Stokes column vector $\mathbf{I}_0$ so that I_0 is the incident energy flux per unit area perpendicular to the beam (we use the definition of the Stokes parameters *I*, *Q*, *U*, and *V* adopted in [18,36]). The Stokes vector **I** of radiation reflected by the medium in the direction $\hat{n}_{\rm obs}$ is given by

$$\mathbf{I} = \frac{1}{\pi}\mu_0 \mathbf{S}(\hat{n}_{\rm obs}, \hat{n}_{\rm ill})\mathbf{I}_0 \tag{1}$$

where μ_0 is the cosine of the zenith angle of the incidence direction and $\mathbf{S}(\hat{n}_{\rm obs}, \hat{n}_{\rm ill})$ is the 4×4 reflection matrix transforming the Stokes parameters of the incident light into those of the reflected light. Note that $\mathbf{I}_0$ and **I** are defined with respect to the meridional planes of the incidence and the scattering direction, respectively.

The reflection matrix can be decomposed as [7]

$$\mathbf{S}(\hat{n}_{\rm obs}, \hat{n}_{\rm ill}) = \mathbf{S}^{\rm 1}(\hat{n}_{\rm obs}, \hat{n}_{\rm ill}) + \mathbf{S}^{\rm L}(\hat{n}_{\rm obs}, \hat{n}_{\rm ill}) + \mathbf{S}^{\rm C}(\hat{n}_{\rm obs}, \hat{n}_{\rm ill}) \tag{2}$$

where 1 denotes the first-order-scattering component, L denotes the ladder component, and C denotes the cyclical component. The first-order-scattering and ladder components of the reflection matrix are rather slowly varying functions of the reflection direction, and their sum describes the diffuse, incoherent background of the reflected radiation. The cyclical component describes the effect of coherent backscattering, which is superposed on the diffuse background. Unlike $\mathbf{S}^{\rm 1}$ and $\mathbf{S}^{\rm L}$, the cyclical component deviates from zero only in the nearest vicinity of the backscattering direction given by $\hat{n}_{\rm obs} = -\hat{n}_{\rm ill}$ and vanishes outside

the coherent backscattering peak.

Both $\mathbf{S}^{1}$ and $\mathbf{S}^{\mathrm{L}}$ can be found by solving numerically the vector radiative transfer equation [16,37–39]. The computation of the cyclical component $\mathbf{S}^{\mathrm{C}}(\hat{n}_{\mathrm{obs}},\hat{n}_{\mathrm{ill}})$ for any $\hat{n}_{\mathrm{ill}}$ and $\hat{n}_{\mathrm{obs}}$ is a much more complicated problem which has been solved rigorously only for the case of nonabsorbing Rayleigh scattering (see the following section) and still awaits a general solution for particles of arbitrary size, shape, and refractive index. However, the rigorous relationship derived in [31,40] and based on Saxon's reciprocity relation for the scattering dyad [41] enables one to use the known ladder component of the reflection matrix for calculating the cyclical component at exactly the backscattering direction, i.e., the matrix $\mathbf{S}^{\mathrm{C}}(-\hat{n}_{\mathrm{ill}},\hat{n}_{\mathrm{ill}})$. Specifically, assuming for simplicity that the scattering medium is macroscopically isotropic and mirror-symmetric [18,36], we have

$$\mathbf{S}^{\mathrm{C}}(-\hat{n}_{\mathrm{ill}},\hat{n}_{\mathrm{ill}})=\begin{bmatrix} S_{11}^{\mathrm{C}}(-\hat{n}_{\mathrm{ill}},\hat{n}_{\mathrm{ill}}) & S_{12}^{\mathrm{L}}(-\hat{n}_{\mathrm{ill}},\hat{n}_{\mathrm{ill}}) & 0 & 0 \\ S_{12}^{\mathrm{L}}(-\hat{n}_{\mathrm{ill}},\hat{n}_{\mathrm{ill}}) & S_{22}^{\mathrm{C}}(-\hat{n}_{\mathrm{ill}},\hat{n}_{\mathrm{ill}}) & 0 & 0 \\ 0 & 0 & S_{33}^{\mathrm{C}}(-\hat{n}_{\mathrm{ill}},\hat{n}_{\mathrm{ill}}) & S_{34}^{\mathrm{L}}(-\hat{n}_{\mathrm{ill}},\hat{n}_{\mathrm{ill}}) \\ 0 & 0 & -S_{34}^{\mathrm{L}}(-\hat{n}_{\mathrm{ill}},\hat{n}_{\mathrm{ill}}) & S_{44}^{\mathrm{C}}(-\hat{n}_{\mathrm{ill}},\hat{n}_{\mathrm{ill}}) \end{bmatrix} \tag{3}$$

where

$$S_{11}^{\mathrm{C}}=\tfrac{1}{2}(S_{11}^{\mathrm{L}}+S_{22}^{\mathrm{L}}-S_{33}^{\mathrm{L}}+S_{44}^{\mathrm{L}}) \tag{4}$$

$$S_{22}^{\mathrm{C}}=\tfrac{1}{2}(S_{11}^{\mathrm{L}}+S_{22}^{\mathrm{L}}+S_{33}^{\mathrm{L}}-S_{44}^{\mathrm{L}}) \tag{5}$$

$$S_{33}^{\mathrm{C}}=\tfrac{1}{2}(-S_{11}^{\mathrm{L}}+S_{22}^{\mathrm{L}}+S_{33}^{\mathrm{L}}+S_{44}^{\mathrm{L}}) \tag{6}$$

$$S_{44}^{\mathrm{C}}=\tfrac{1}{2}(S_{11}^{\mathrm{L}}-S_{22}^{\mathrm{L}}+S_{33}^{\mathrm{L}}+S_{44}^{\mathrm{L}}) \tag{7}$$

[the arguments $(-\hat{n}_{\mathrm{ill}},\hat{n}_{\mathrm{ill}})$ are omitted for brevity]. Thus, the combined use of the vector radiative transfer theory and Eqs. (2)–(7) provides the full specification of the reflected radiation outside the peak [Eq. (2) with $\mathbf{S}^{\mathrm{C}}(\hat{n}_{\mathrm{obs}},\hat{n}_{\mathrm{ill}})=0$] and at exactly the center of the backscattering peak.

Equations (3)–(7) represent one of a very few rigorous results of the vector theory of coherent backscattering by sparsely distributed, independently scattering particles and are an important source of benchmark theoretical results for arbitrary particles. Mishchenko [15,16,31] used this formulation to perform a detailed study of the analytical properties of various photometric and polarimetric characteristics of coherent backscattering and their qualitative and quantitative dependence on the particle size, shape, and refractive index. Extensive applications of this approach to model computations and analyses of

laboratory and remote-sensing data are described in [9–11,16]. In particular, numerical calculations for specific scattering systems [40] show excellent quantitative agreement with the results of controlled laboratory experiments reported in [42,43].

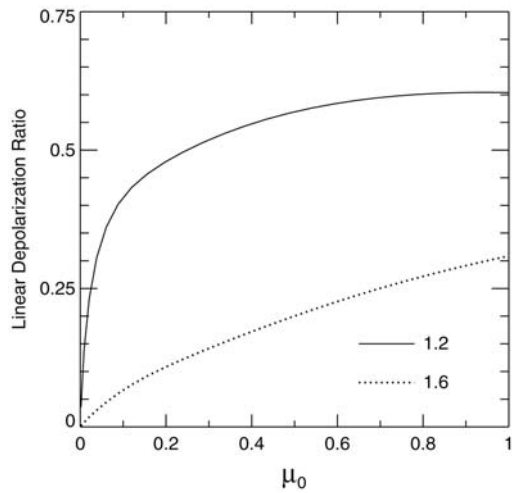

Figure 4: Linear depolarization ratio versus cosine of the incident zenith angle for backscattering by a semi-infinite homogeneous layer composed of polydisperse spherical particles with an effective size parameter of 10 and refractive indices 1.2 and 1.6.

As an example, Fig. 4 shows the linear depolarization ratio δ_{L} (also known in the radar literature as the linear polarization ratio μ_{L}) versus μ_0 for a semi-infinite layer composed of spherical particles [16]. δ_{L} is defined assuming that the incident light is linearly polarized parallel to the meridional plane of the incidence direction and is the ratio of the two orthogonal components of the total backscattered intensity: one polarized in the direction perpendicular to the meridional plane and the other polarized parallel to the plane. A deviation of δ_{L} from zero means that the backscattered light is partially depolarized. It is seen that δ_{L} is zero in the limit $\mu_0 \to 0$, i.e., when only the light scattered once contributes to the total reflected signal. This first-order-scattering contribution is not depolarized because the particles forming the medium are spherical [18]. However, for normal incidence ($\mu_0 = 1$) the multiple-scattering contribution to the total backscattered signal is significant and results in strong depolarization. Figure 5 shows analogous results for the circular depolarization ratio δ_{C} (also known as the circular polarization ratio μ_{C}). The latter is introduced assuming that the incident light is circularly polarized and is the ratio of two circular components of the total intensity of

the backscattered light: one polarized in the same direction as the incident light and the other polarized in the opposite direction. Since for single scattering by a spherical particle $\delta_C \equiv 1$ [18], the large δ_C values shown in Fig. 5 for $\mu_0 \neq 0$ demonstrate a strong depolarizing effect of multiple scattering. The numerical results reported in [15,16] suggest that $\delta_L \leq 1$ and $\delta_C \geq \delta_L$. These properties of the depolarization ratios produced by multiple scattering are similar to those of the depolarization ratios caused by single scattering on nonspherical particles [18,36]. This factor can make it difficult in practice to distinguish between the two depolarization mechanisms.

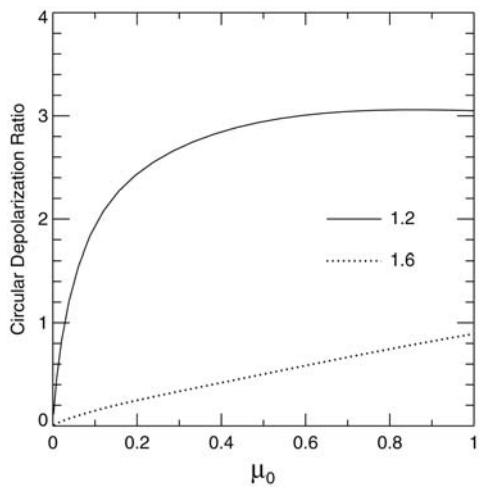

Figure 5: As in Fig. 4, but for the circular depolarization ratio.

Radar observations of icy outer planet satellites at centimeter wavelengths show that when illuminated and observed in linearly polarized radiation, $\delta_L \approx 0.5$, whereas when illuminated and observed in circularly polarized radiation, $\delta_C > 1$ [44,45]. The results of [15,16] show that the observed values of the depolarization ratios can be adequately explained by multiple scattering and localization of light in weakly absorbing discrete random media.

3. Conservative Rayleigh scattering

Another important exact result of the vector theory of coherent backscattering is the complete analytical solution for the case of normal incidence of light on a semi-infinite slab composed of nonabsorbing Rayleigh scatterers. This solution was first obtained by Ozrin [32] and was then re-derived in a more convenient form by Amik *et al.* [46].

Restricting the analysis to small phase angles α, where the first-order-scattering and ladder components of the total reflection matrix are

approximately constant, and introducing the so-called angular parameter $q = kl\alpha$, where l is the photon transport mean free path in the scattering medium, one can rewrite the main formulas of [46] using the Stokes-vector representation of polarization as follows [47]:

$$\mathbf{S}^{1} = \tfrac{3}{16}\,\mathrm{diag}[1, 1, -1, -1] \tag{8}$$

$$\mathbf{S}^{\mathrm{L}} = \tfrac{1}{4}\,\mathrm{diag}[\gamma_{11}(0)+\gamma_{12}(0), \gamma_{11}(0)-\gamma_{12}(0), \gamma_{12}(0)-\gamma_{11}(0), \gamma_{44}(0)] - \mathbf{S}^{1} \tag{9}$$

$$\mathbf{S}^{\mathrm{C}}(q) = \begin{bmatrix} \tilde{S}_{11}(q) & \tilde{S}_{12}(q) & 0 & 0 \\ \tilde{S}_{12}(q) & \tilde{S}_{22}(q) & 0 & 0 \\ 0 & 0 & \tilde{S}_{33}(q) & 0 \\ 0 & 0 & 0 & \tilde{S}_{44}(q) \end{bmatrix} - \mathbf{S}^{1} \tag{10}$$

where

$$\tilde{S}_{11}(q) = \tfrac{1}{8}[\gamma_{11}(q)+\gamma_{22}(q)-\gamma_{33}(q)+\gamma_{44}(q)] \tag{11}$$

$$\tilde{S}_{22}(q) = \tfrac{1}{8}[\gamma_{11}(q)+\gamma_{22}(q)+\gamma_{33}(q)-\gamma_{44}(q)] \tag{12}$$

$$\tilde{S}_{33}(q) = \tfrac{1}{8}[\gamma_{33}(q)+\gamma_{44}(q)] - \tfrac{1}{4}\gamma_{12}(q) \tag{13}$$

$$\tilde{S}_{44}(q) = \tfrac{1}{8}[\gamma_{33}(q)+\gamma_{44}(q)] + \tfrac{1}{4}\gamma_{12}(q) \tag{14}$$

$$\tilde{S}_{12}(q) = \tfrac{1}{8}[\gamma_{11}(q)-\gamma_{22}(q)] \tag{15}$$

Since the angular functions $\gamma_{ij}(q)$ can be computed numerically as described in detail in [46], Eqs. (2) and (8)–(15) can be used to calculate the full Stokes reflection matrix for any q. If, furthermore, the transport mean free path l is known, the reflection matrix can be expressed as a function of the phase angle α rather than the dimensionless angular parameter q. Note that the matrices $\mathbf{S}^{\mathrm{L}}$ and $\mathbf{S}^{\mathrm{C}}(0)$ given by Eqs. (9)–(15) fully comply with the general relationship derived for arbitrary macroscopically isotropic and mirror-symmetric scattering media and discussed in the previous section.

Assuming unpolarized incident light ($Q_0 = U_0 = V_0 = 0$), we define the intensity enhancement factor as the ratio of the total reflected intensity to the incoherent background value:

$$\zeta(q) = \frac{S_{11}^{1} + S_{11}^{\mathrm{L}} + S_{11}^{\mathrm{C}}(q)}{S_{11}^{1} + S_{11}^{\mathrm{L}}} \tag{16}$$

Equations (8)–(10) show that only the first two Stokes parameters of the

reflected light can be nonzero. Therefore the degree of linear polarization can be defined as minus the ratio of the total reflected second Stokes parameter to the total reflected intensity:

$$P(q) = -\frac{Q(q)}{I(q)} = -\frac{S_{12}^{\mathrm{C}}(q)}{S_{11}^{1} + S_{11}^{\mathrm{L}} + S_{11}^{\mathrm{C}}(q)} \tag{17}$$

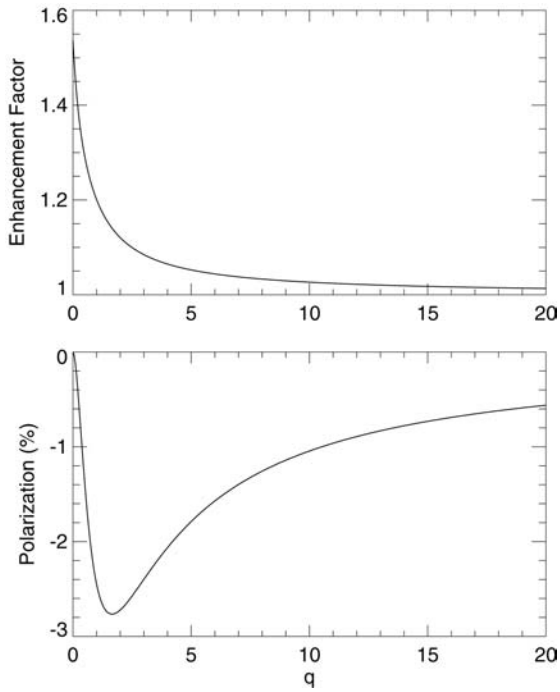

Figure 6: Angular profiles of the photometric enhancement factor and the degree of linear polarization of the reflected light for a half-space of nonabsorbing Rayleigh particles.

Figure 6 shows both the intensity enhancement factor and the degree of linear polarization as functions of the dimensionless angular parameter q [47]. The upper panel demonstrates the renowned intensity peak centered at exactly the opposition. The amplitude of the peak is $\zeta(0) \approx 1.5368$ and its half-width at half-maximum is $q_{\zeta} \approx 0.597$. Thus the relationship between the half-width at half-maximum of the backscattering intensity peak and the photon transport mean free path is given by $\alpha_{\zeta} \approx 0.597/kl$. The lower panel of Fig. 6 shows that the reflected polarization is zero at opposition, which is a consequence of azimuthal symmetry in the case of normal illumination and unpolarized incident light. However, with increasing q, polarization becomes negative, rapidly grows in absolute value, and reaches its minimal value

$P_{\min} \approx -2.765\%$ at a reflection direction very close to opposition ($q_P \approx 1.68$). The peak of negative polarization is highly asymmetric so that the half-minimal polarization value –1.383% is first reached at $q_{P,1} \approx 0.498$, which is even smaller than the value $q_\zeta \approx 0.597$ corresponding to the half-width at half-maximum of the backscattering intensity peak, and then at a much larger $q_{P,2} \approx 7.10$. This unusual behavior of polarization at near-backscattering angles was called in [11] the (asymmetric) polarization opposition effect (POE).

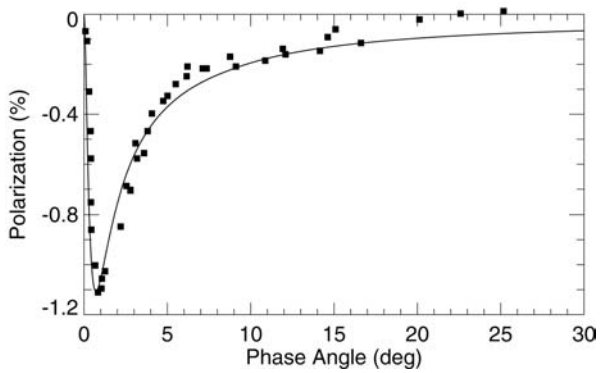

Figure 7: Polarization measurements for a particulate surface composed of microscopic magnesia particles (squares) and best-fit theoretical computations (solid curve).

Because lasers are the most frequently used source of illumination and usually generate linearly or circularly polarized light, explicit laboratory demonstrations of the sharp and asymmetric POE have been extremely rare. Apparently the first laboratory observation of the asymmetric POE was made by Lyot as long ago as in the 1920s [48], even though the physical explanation of this phenomenon was, of course, unknown at that time. Figure 7 shows Lyot's polarization measurements for a particulate surface obtained by burning a tape of magnesium under a glass plate until the deposit on the plate was completely opaque. Lyot described the observed polarization phase curve as "puzzling" and attributed it to the very small size of magnesia grains. Unfortunately, he did not measure the actual size of the grains and their packing density and thus did not provide the information necessary to compute the photon mean free path *l*. Furthermore, the minimal measured polarization value is only –1.11%, compared to the theoretical value $P_{\min} \approx -2.765\%$ computed for Rayleigh particles. However, assuming that the latter difference is explained by the finite particle size in Lyot's experiment and multiplying the theoretical polarization by a factor of 0.4, and also assuming that the actual *kl* was close to a realistic value of 132, it is possible to reproduce almost perfectly the angular profile of the measured polarization up to phase angles of

about 15° (solid curve in Fig. 7) [47]. At larger phase angles the assumption of phase-angle-independent single-scattering and ladder contributions to the total reflection matrix is no longer valid and causes a significant deviation of the theoretical curve from the measurements.

The sharp asymmetric POE also may have been observed in more recent laboratory measurements by Geake and Geake [49] for fine alumina powders, although the smallest phase angle in their experiments was 2° and may be too large for deriving definitive conclusions. These measurements may suggest that the narrow asymmetric POE weakens and ultimately disappears with increasing particle size, which would be consistent with the similar disappearance of the spatial anisotropy of the backscattering intensity peak in the case of a linearly polarized incident beam observed by van Albada *et al*. [28].

Sharp asymmetric peaks of negative polarization at phase angles considerably smaller than 1° have been observed for Saturn's rings and the Galilean satellites of Jupiter [11,50; see also the chapter by Rosenbush *et al.*]. Because these peaks are distinctly different from the symmetric, nearly parabolic negative polarization branch commonly observed for many solar system bodies [51], they have been interpreted in terms of the asymmetric POE produced by coherent backscattering of sunlight by a surface layer composed primarily of microscopic ice particles [11,50]. The fact that the same objects exhibit comparably narrow intensity peaks centered at exactly the opposition [52] provides strong support for this interpretation.

4. Scattering by a plane-parallel layer composed of arbitrary particles in random orientation

In this section we consider multiple scattering by a plane-parallel layer consisting of discrete, randomly positioned scatterers in random orientation. As in the preceding section, the incident wave is assumed to propagate normally to the boundary of the medium. A comprehensive derivation of the equations describing the coherent and incoherent (diffuse) parts of radiation reflected by such a medium at the backscattering direction was given in [53]. It is based on the exact theory of electromagnetic scattering by systems (clusters) of particles. The equations derived allow a detailed study of the dependence of the photometric and polarization opposition effect characteristics on the microphysical properties of the scatterers (size parameter, real and imaginary parts of the refractive index, shape, number density, etc.). Here we present a brief summary of these results.

The reflection matrix is decomposed according to Eq. (2). The sum of the first-order-scattering and ladder components of the reflection matrix is given by

$$S^{1}_{pn\mu\nu} + S^{\mathrm{L}}_{pn\mu\nu} = \frac{-n_0}{2k^3\cos\vartheta}\sum_l d^l_{M_0N_0}(\vartheta)\int_0^{kZ_0}\exp\left(2z\frac{\mathrm{Im}(\varepsilon)}{\cos\vartheta}\right)\alpha_l^{(z)(pn)(\mu\nu)}dz \qquad (18)$$

where the matrix elements $S^{1}_{pn\mu\nu}$ and $S^{\mathrm{L}}_{pn\mu\nu}$ are written in terms of the circular-polarization (CP) representation of the Stokes vector [54], n_0 is the particle number density, $p, n, \mu, \nu = \pm 1$, $d^l_{M_0N_0}(\vartheta)$ are Wigner d functions [55] ($M_0 = \nu - n$, $N_0 = \mu - p$), ϑ is the scattering angle (the angle between the incidence and scattering directions), Z_0 is the geometrical thickness of the layer, and ε is the complex effective refractive index of the medium. The expansion coefficients $\alpha_L^{(z)(pn)(\mu\nu)}$ are determined from the system of equations

$$\alpha_L^{(z)(pn)(\mu\nu)} = \chi_L^{(pn)(\mu\nu)}\exp(-\tau_z) + \frac{2\pi n_0}{k^3}\sum_{qq_1}\chi_L^{(pq)(\mu q_1)}$$
$$\times\int\sum_l \alpha_L^{(y)(qn)(q_1\nu)}\exp(-\tau_\rho)d^L_{M_0N}(\omega)d^l_{M_0N}(\omega)d\rho\sin\omega d\omega \qquad (19)$$

where ρ, ω are polar coordinates of the integration point with respect to the point z, the angle ω is measured off the backscattering direction, $\tau_x = 2\,\mathrm{Im}(\varepsilon)x$, $N = q_1 - q$ ($q, q_1 = \pm 1$), and $y = z - \rho\cos\omega$. The $\chi_L^{(pn)(\mu\nu)}$ are the coefficients in the expansion of the individual-particle scattering matrix in the Wigner d functions, and the first term on the right-hand side corresponds to the first-order-scattering contribution.

Equation (19) specifies the coefficients $\alpha_L^{(z)(pn)(\mu\nu)}$ as functions of the optical depth in the layer. The exponential factor in Eq. (18) describes the extinction of radiation while it propagates from a point z to the exit point in the direction ϑ. Note that Eqs. (18) and (19) are one of many alternative representations of the vector radiative transfer equation.

The cyclical component of the reflection matrix can be written as

$$S^{\mathrm{C}}_{pn\nu\mu} = \frac{-n_0}{2k^3\cos\vartheta}\int_0^{kZ_0} G^{(z)(pn)(\mu\nu)}\exp\left(-2z\,\mathrm{Im}(\varepsilon)\left(1-\frac{1}{\cos\vartheta}\right)\right)dz \qquad (20)$$

where the matrix $G^{(z)(pn)(\mu\nu)}$ is defined by

$$G^{(z)(pn)(\mu\nu)} = \frac{2\pi n_0}{k^3}\sum_{qq_1LM}(-1)^L\zeta^{*(q_1\mu)(qp)}_{LM}\int\sum_{lm}\beta_{lm}^{(y)(qn)(q_1\nu)}$$
$$\times d^L_{MN}(\omega)d^l_{mN}(\omega)\exp(-\tilde{\tau}_\rho)F_{m-M}(\rho,\vartheta,\omega)d\rho\sin\omega d\omega \qquad (21)$$

Here $\zeta_{LM}^{(pn)(\mu\nu)}$ are the coefficients in the expansion of the phase matrix elements in the Wigner d functions,

$$F_m(\rho,\vartheta,\omega)=\sum_l i^{-l}(2l+1)j_l\left(2\rho\cos\frac{\vartheta}{2}\right)d^l_{m0}\left(\frac{\vartheta}{2}\right)d^l_{m0}(\omega)$$
$$=i^{-m}J_m(\rho\sin\vartheta\sin\omega)\exp(-i\rho\cos\omega(1+\cos\vartheta)) \quad (22)$$

$$\tilde{\tau}_\rho=\rho\,\mathrm{Im}(\varepsilon)\left(2-\cos\omega\left(1-\frac{1}{\cos\vartheta}\right)\right)+i\rho\cos\omega[\mathrm{Re}(\varepsilon)-1]\left(1+\frac{1}{\cos\vartheta}\right) \quad (23)$$

$j_l(x)$ are spherical Bessel functions, and $J_m(x)$ are Bessel functions. The coefficients $\beta^{(z)(pn)(\mu\nu)}_{LM}$ are determined from the system of equations

$$\beta^{(z)(pn)(\mu\nu)}_{LM}=\zeta^{(pn)(\mu\nu)}_{LM}+\frac{2\pi n_0}{k^3}\sum_{qq_1}\chi^{(pq)(\mu q_1)}_L\int\sum_{lm}\beta^{(y)(qn)(q_1\nu)}_{lm}$$
$$\times d^L_{MN}(\omega)d^l_{mN}(\omega)\exp(-\tilde{\tau}_\rho)F_{m-M}(\rho,\vartheta,\omega)d\rho\sin\omega d\omega \quad (24)$$

The matrix $S^{\mathrm{C}}_{pn\nu\mu}$ describes the interference of the conjugate pairs of waves propagating along the same trajectories (Fig.1) including looped paths [53,56].

The above equations are rigorous provided that any scatterer is located in the far-field zone of all other scatterers. They are valid for arbitrary particles in random orientation. Unlike the formula for the incoherent part, Eq. (19), the kernel of the formula for the coherent part, Eq. (24), is a rapidly oscillating function. The numerical solution of such equations is a very complex problem. Therefore, below we consider several particular cases of the general equations.

4.1 Exact backscattering direction ($\vartheta=\pi$)

In this case $F_m(\rho,\pi,\omega)=\delta_{0m}$ and $\zeta^{*(\nu\mu)(np)}_{LM}=(-1)^p\chi^{(pn)(\mu\nu)}_L\delta_{M,-N_0}$. Therefore, Eqs. (18), (19), and (20)–(24) yield [53]

$$S^{\mathrm{L}}_{pn\mu\nu}=S^{\mathrm{C}}_{pn\nu\mu} \quad (25)$$

Rewriting Eq.(25) in terms of the standard Stokes representation of polarization gives Eqs. (4)–(7) [56].

It should be noted that the relations between the coherent and incoherent parts of the reflected radiation similar to Eqs. (4)–(7) and (25) can be derived for an arbitrary system of scatterers provided that they are in the far-field zones of each other. It can be done using Eqs. (19), (20), (35), and (36) of [53].

4.2 Double-scattering approximation for a semi-infinite layer

The results of the double-scattering approximation are useful for semi-quantitative or qualitative analyses of the effect of particle microphysical properties on the characteristics of the opposition effects. Instead of Eqs. (18) and (19), we now have the following [56]:

$$S^{1}_{pn\mu\nu} + S^{\mathrm{L}}_{pn\mu\nu} = \frac{n_0}{4k^3\,\mathrm{Im}(\varepsilon)(1-\cos\vartheta)}\sum_l d^l_{M_0N_0}(\vartheta)A_l^{(pn)(\mu\nu)} \tag{26}$$

where

$$\begin{aligned} A_L^{(pn)(\mu\nu)} &= \chi_L^{(pn)(\mu\nu)} + \frac{\pi n_0}{k^3 Im(\varepsilon)}\sum_{qq_1}\chi_L^{(pq)(\mu q_1)}\sum_l \chi_l^{(qn)(q_1\nu)} \\ &\times\left[\int_0^{\pi/2} d^L_{M_0N}(\omega)d^l_{M_0N}(\omega)\frac{\cos\vartheta\sin\omega d\omega}{\cos\vartheta-\cos\omega}\right. \\ &\left.+\int_0^{\pi/2} d^L_{M_0N}(\pi-\omega)d^l_{M_0N}(\pi-\omega)\frac{\sin\omega d\omega}{1+\cos\omega}\right] \end{aligned} \tag{27}$$

The first term on the right-hand side of Eq. (27) gives the first-order-scattering contribution, whereas the second one describes the second-order-scattering contribution. The coherent part for a semi-infinite layer is given by [56]

$$S^{\mathrm{C}}_{pn\nu\mu} = \frac{\pi n_0^2}{2k^6\,\mathrm{Im}(\varepsilon)(1-\cos\vartheta)}\sum_{LMlmqq_1}(-1)^L\zeta^{*(q_1\mu)(qp)}_{LM}\zeta^{(qn)(q_1\nu)}_{lm}i^{-|m-M|}B^{(qq_1)}_{LMlm} \tag{28}$$

where

$$\begin{aligned} B^{(qq_1)}_{LMlm} &= \int_0^{\pi/2} d^L_{MN}(\omega)d^l_{mN}(\omega)\frac{c^{|m-M|}\sin\omega d\omega}{\sqrt{c^2+f^2}\,(f+\sqrt{c^2+f^2})^{|m-M|}} \\ &+\int_0^{\pi/2} d^L_{MN}(\pi-\omega)d^l_{mN}(\pi-\omega)\frac{c^{|m-M|}\sin\omega d\omega}{\sqrt{c^2+f^{*2}}\,(f^*+\sqrt{c^2+f^{*2}})^{|m-M|}} \end{aligned} \tag{29}$$

$$c = \sin\vartheta\sin\omega \tag{30}$$

$$f = 2\,\mathrm{Im}(\varepsilon)+\cos\omega\left\{\mathrm{Im}(\varepsilon)\left(1-\frac{1}{\cos\vartheta}\right)+i[\mathrm{Re}(\varepsilon)-1]\left(1+\frac{1}{\cos\vartheta}\right)+i(1+\cos\vartheta)\right\} \tag{31}$$

The expansion coefficients $\chi_L^{(pn)(\mu\nu)}$ and $\zeta_{LM}^{(pn)(\mu\nu)}$ are determined by the microphysical properties of the scatterers. In the case of spherical particles,

$$\chi_{L_1}^{(pn)(\mu\nu)} = \frac{1}{4}\sum_{Ll}(2L+1)(2l+1)\langle a_L^{(pn)}a_l^{*(\mu\nu)}\rangle C^{L_1M_0}_{L-nl\nu}C^{L_1N_0}_{L-pl\mu} \tag{32}$$

$$\zeta_{L_1M_1}^{(pn)(\mu\nu)} = \frac{1}{4}\sum_{Ll}(2L+1)(2l+1)\langle a_L^{(pn)}a_l^{*(\mu\nu)}\rangle C^{L_1M_1}_{L-nlm_1}C^{L_1N_0}_{L-pl\mu}(-1)^l d^l_{m_1-\nu}(\vartheta) \tag{33}$$

where $m_1 = M_1 + n$, $a_L^{(pn)} = a_L + pnb_L$, a_L and b_L are the Lorenz–Mie coefficients [18], the angle brackets denote averaging over particle microphysical characteristics, and the *C*s are Clebsh-Gordan coefficients [55].

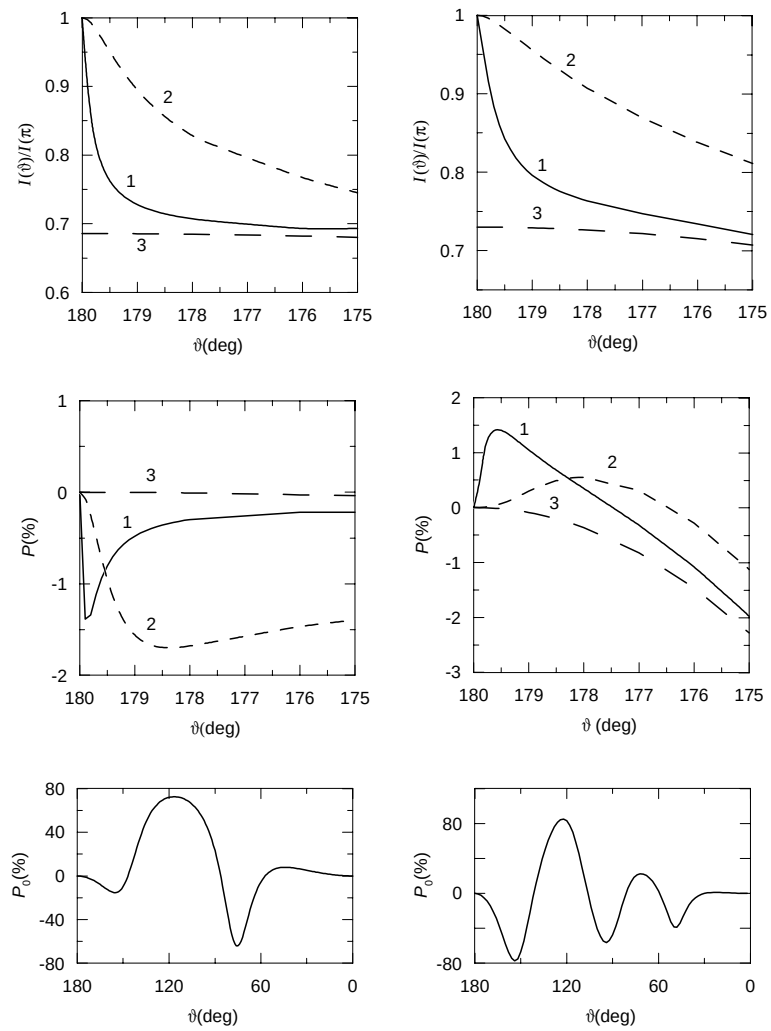

Figure 8: The coherent component (1, 2) and the sum of the diffuse and first-order-scattering components (3) of the scattered radiation for ka = 3, m = 1.35 (left-hand column) and ka = 4.5, m = 1.33 (right-hand column). Curves 1 correspond to ξ =0.001; curves 2 correspond to ξ =0.01. P_0 is the linear polarization for an individual isolated particle.

Figure 8 depicts the degree of linear polarization, P, and the normalized intensity, $I(\vartheta)/I(\pi)$, for a semi-infinite layer composed of identical spherical particles. The results are shown for different values of the filling factor $\xi = \frac{4}{3}\pi a^3 n_0$, where a is the particle radius. The effective refractive index of the medium is given by $\varepsilon = 1 + i n_0 C_{\text{ext}}/2k$, where C_{ext} is the extinction cross section per particle.

One can see that the polarization opposition effect is more sensitive to particle properties than the photometric one (the latter always manifests itself as a sharp peak of intensity centered at the exact backscattering direction). The polarization behavior can be explained as follows. It has been demonstrated that in the case of positive polarization for an isolated scatterer, the interference of second-order waves results in negative polarization at the backscattering direction [4]. However uniformly positive polarization is a specific property of Rayleigh scatterers. The angular dependence of polarization for wavelength-sized particles becomes much more complicated [18]. Therefore, the interference of the second-order waves can result in positive backscattering polarization as well as in negative polarization.

The left-hand column of Fig. 8 corresponds to spherical particles with a size parameter $x = ka = 3$ and a refractive index m = 1.35. The phase function for these particles is asymmetric, most of radiation being scattered at angles $\vartheta < 60°$. Therefore, the polarization of the coherent part of the reflected radiation is determined by the behavior of P_0 in the scattering-angle ranges $\vartheta < 60°$ and $\vartheta > 120°$, where the average value of P_0 is positive (see the bottom panel of the left-hand column of Fig. 8). Hence, the interference of second-order scattering paths yields negative polarization near the opposition direction.

The right-hand column of Fig. 8 corresponds to particles with a size parameter $x = 4.5$ and a refractive index m = 1.33. The phase function for these particles is even more asymmetric. The average value of P_0 in the scattering-angle ranges $\vartheta < 60°$ and $\vartheta > 120°$ is negative. In this case the interference of the second-order scattering paths results in positive polarization at backscattering angles.

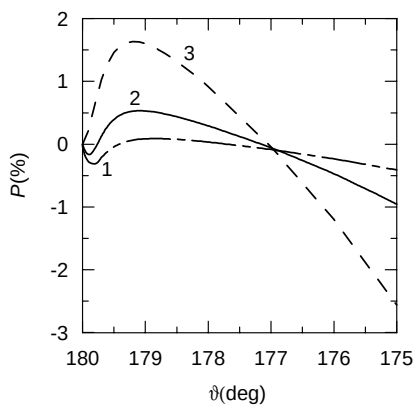

Figure 9: Degree of linear polarization for a semi-infinite particulate layer with ξ = 0.002 and different parameters of the particle size distribution. Curve 1: $x_{\rm eff}$ = 2, $v_{\rm eff}$ = 0.1; curve 2: $x_{\rm eff}$ = 2, $v_{\rm eff}$ = 0.25; curve 3: $x_{\rm eff}$ = 3, $v_{\rm eff}$ = 0.25.

Figures 9 and 10 show the polarization profiles for a gamma-distribution of particle size parameters $f(x) \propto x^{(1-3v_{\rm eff})/v_{\rm eff}} \exp[-x/(x_{\rm eff} v_{\rm eff})]$, where $x_{\rm eff}$ is the

effective size parameter and v_{eff} is the effective variance, and refractive indices 1.5 and 1.33 + 0.05*i*, respectively. One can see that varying polarization behavior is possible depending on particle parameters. In particular, the degree of linear polarization at small phase angles can be negative as well as positive, and it is possible to obtain a bimodal angular dependence. The bimodal polarization behavior in Fig. 10 (curve 1) is formed by a superposition of the sharp polarization peak formed by constructive interference of waves scattered by different scatterers and the smooth polarization minimum caused by single scattering.

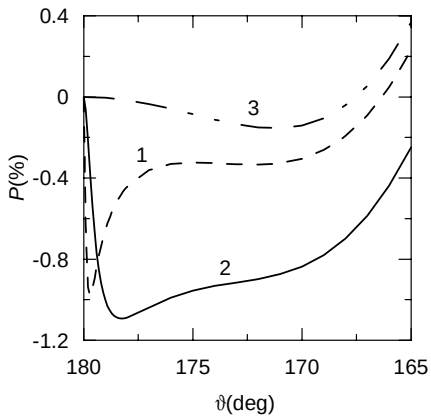

Figure 10: Degree of linear polarization for a semi-infinite layer composed of polydisperse spherical particles with x_{eff} = 2 and v_{eff} = 0.1. Curves 1 and 2 show the coherent component; curve 3 shows the sum of the first-order-scattering and diffuse components. Curve 1 corresponds to $\xi = 0.002$, curve 2 – to $\xi = 0.01$.

4.3 Optically thin layers

Figures 8–10 show a strong influence of particle microphysics and filling factor on polarization, in particular on the angular position of the polarization extremum α_m. The angular position of the extremum can be an important characteristic in analyses of experimental data. In the case of an optically thin layer, the integral over ρ in Eq. (21) is a sharp function, which has a maximum at $\omega = \pi/2$ and tends to zero for other values of ω. For such a layer composed of moderately sized particles, the scattering-angle dependence of the coefficients $\zeta_{LM}^{(np)(v\mu)}$ at $\vartheta \to \pi$ is weak. Moreover, we can now neglect all orders of scattering higher then the second. This allows us to derive an analytical expression for α_m:

$$\frac{\sin\alpha_m}{2\,\mathrm{Im}(\varepsilon)} = kl\sin\alpha_m = \sqrt{\sqrt{2}(2+\sqrt{2})} \approx 2 \tag{34}$$

where l is the photon transport mean free path. This expression agrees well with that for a semi-infinite layer composed of nonabsorbing point-like scatterers (Section 3). In both cases α_m is defined only by the value of l.

Equation (34) can be used in analyses of remote-sensing observations, for example, for estimating surface properties of particles forming Saturn's rings. The majority of the ring particles are believed to have sizes ranging from a few centimeters to a few meters and surface morphology similar to that of snow or frost [57]. A recent analysis of numerous earth-based observations shows a bimodal phase-angle dependence of linear polarization of light reflected by Saturn's rings and Galilean satellites of Jupiter [50]. The value of α_m for the first (sharp) polarization minimum is about $0.5°$, whereas the one for the second (smooth) minimum is about $3° - 4°$. One potential explanation of this bimodal behavior is that the smooth polarization minimum is produced by cooperative scattering within wavelength-sized aggregates consisting of a modest number of small components, whereas the sharp polarization peak is the result of constructive interference of waves scattered by different aggregates. The filling factors of aggregates then follows from

$$\xi = \frac{2\pi\langle x\rangle^3 \alpha_m}{3k^2 C_{\text{sca}}(1-\langle\cos\vartheta\rangle)} \tag{35}$$

where C_{sca} is the scattering cross section per aggregate, $\langle\cos\vartheta\rangle$ is the asymmetry parameter, and $\langle x\rangle$ is the average size parameter of the aggregates. Numerical calculations using Eqs. (35) for refractive indices $1.2 \div 1.33$ and $5 \le \langle x\rangle \le 20$ give $\xi \cong 0.02 \div 0.3$. The smooth negative polarization minimum can be produced by aggregates consisting of 10^2 to 10^3 monomers with size parameters $\cong 0.1$, which implies $\langle x\rangle \cong 10$ and $\xi \cong 0.1$. These estimates assume that the size of the aggregates relative to the wavelength and their packing density are small enough so that the effects of shadowing can be ignored. Of course, another possible explanation is that the surfaces of these objects are highly heterogeneous and that the sharp negative polarization minimum is produced by the areas covered with an optically thick layer of microscopic (Rayleigh) grains (Section 3), whereas the smooth polarization minimum is produced by the areas covered by particles of a different type.

5. Acknowledgments

M. Mishchenko acknowledges support from the NASA Radiation Sciences Program managed by Donald Anderson and from the NASA Earth Observing System program. V. Tishkovets and P. Litvinov appreciate funding received under INTAS Grant No. 1999-00652.

References

1. Yu. G. Shkuratov, Kinem. Fiz. Nebes. Tel **4**, 33 (1988).
2. K. Muinonen, Ph.D. thesis, Univ. Helsinki (1990).
3. B. Hapke, Icarus **88**, 407 (1990).
4. Yu. G. Shkuratov, Astron. Vestnik **25**, 152 (1991).
5. M. Nieto-Vesperinas and J. C. Dainty (Eds.), "Scattering in Volumes and Surfaces" (North-Holland, Amsterdam, 1990).
6. P. Sheng (Ed.), "Scattering and Localization of Classical Waves in Random Media" (World Scientific, Singapore, 1990).
7. Yu. N. Barabanenkov, Yu. A. Kravtsov, V. D. Ozrin, A. I. Saichev A. I., Progr. Opt. **29**, 65 (1991).
8. A. Lagendijk, and B. A. van Tiggelen, Phys. Rep. **270**, 143 (1996).
9. M. I. Mishchenko and J. M. Dlugach, Mon. Not. R. Astron. Soc. **254**, 15P (1992).
10. M. I. Mishchenko and J. M. Dlugach, Planet. Space Sci. **41**, 173 (1993).
11. M. I. Mishchenko, Astrophys. J. **411**, 351 (1993).
12. S. J. Ostro, D. B. Campbell, R. A. Simpson, et al., J. Geophys. Res. **97**, 18227 (1992).
13. A. Campbell, R. E. Arvidson, and M. K. Shepard, J. Geophys. Res. **98**, 17099 (1993).
14. B. J. Butler, D. O. Muhleman, and M. A. Slade, J. Geophys. Res. **98**, 15003 (1993).
15. M. I. Mishchenko, Earth Moon Planets **58**, 127 (1992).
16. M. I. Mishchenko, J. Quant. Spectrosc. Radiat. Transfer **56**, 673 (1996).
17. M. I. Mishchenko, Astrophys. Space Sci. **194**, 327 (1992).
18. M. I. Mishchenko, L. D. Travis, and A. A. Lacis, "Scattering, Absorption, and Emission of Light by Small Particles" (Cambridge University Press, Cambridge, 2002).
19. V. P. Tishkovets, Opt. Spectrosc. **85**, 212 (1998).
20. V. P. Tishkovets and P. V. Litvinov, Solar Syst. Res. **33**, 186 (1999).
21. V. P. Tishkovets, Yu. G. Shkuratov, and P. V. Litvinov, J. Quant. Spectrosc. Radiat. Transfer **61**, 767 (1999).
22. K. Muinonen, Proc. 1989 URSI Electromagn. Theory Symp., p. 428 (1989); F. M. Ismagilov and Yu. A. Kravtsov, Waves in Random Media **3**, 17 (1993).
23. M. I. Mishchenko, Opt. Lett. **21**, 623 (1996).
24. M. P. van Albada, M. B. van der Mark, and A. Lagendijk, Phys. Rev. Lett. **58**, 361 (1987).
25. M. B. van der Mark, M. P. van Albada, and A. Lagendijk, Phys. Rev. B **37**, 3575 (1988).
26. E. Akkermans, P. E. Wolf, R. Maynard, and G. Maret, J. Phys. (Paris) **49**, 77 (1988).
27. K. J. Peters, Phys. Rev. B **46**, 801 (1992).
28. M. P. van Albada, M. B. van der Mark, and A. Lagendijk, J. Phys. D **21**, S28 (1988).
29. M. P. van Albada and A. Lagendijk, Phys. Rev. B **36**, 2353 (1987).
30. C. MacKintosh and S. John, Phys. Rev. B **37**, 1884 (1988).
31. M. I. Mishchenko, J. Opt. Soc. Am. A **9**, 978 (1992).
32. V. D. Ozrin, Waves in Random Media **2**, 141 (1992).
33. M. P. van Albada and A. Lagendijk, Phys. Rev. B. **36**, 2353 (1987).
34. S. Martinez and R. Maynard, Phys. Rev. B **50**, 3714 (1994).
35. T. Iwai, H. Furukawa, and T. Asakura, Opt. Rev. **2**, 413 (1995).
36. M. I. Mishchenko, J. W. Hovenier, and L. D. Travis (Eds.), "Light Scattering by Nonspherical Particles: Theory, Measurements, and Applications" (Academic Press, San Diego, 2000).
37. S. Chandrasekhar, "Radiative Transfer" (Clarendon Press, London, 1950).

38. J. E. Hansen and L. D. Travis, Space Sci. Rev. **16**, 527 (1974).
39. J. F. de Haan, P. W. Bosma, and J. W. Hovenier, Astron. Astrophys. **183**, 371 (1987).
40. M. I. Mishchenko, Phys. Rev. B **44**, 12597 (1991).
41. D. S. Saxon, Phys. Rev. **100**, 1771 (1955).
42. M. P. van Albada, M. B. van der Mark, and A. Lagendijk, J. Phys. D **21**, S28 (1988).
43. P. E. Wolf, G. Maret, E. Ackermans, and R. Maynard, J. Phys. (Paris) **49**, 63 (1988).
44. S. Ostro, in D. Morrison (Ed.), "Satellites of Jupiter," p. 213 (University of Arizona Press, Tucson, AZ, 1982).
45. S. J. Ostro, Rev. Mod. Phys. **65**, 1235 (1993).
46. E. Amic, J. M. Luck, and Th. M. Nieuwenhuizen, J. Phys. I **7**, 445 (1997).
47. M. I. Mishchenko, J.-M. Luck, and T. M. Nieuwenhuizen, J. Opt. Soc. Am. A **17**, 888 (2000).
48. B. Lyot, NASA Tech. Transl. F-187 (NASA, Washington, D. C., 1964).
49. J. E. Geake and M. Geake, Mon. Not. R. Astron. Soc. **245**, 46 (1990).
50. V. K. Rosenbush, V. V. Avramchuk, A. E. Rosenbush, and M. I. Mishchenko, Astrophys. J. **487**, 402 (1997).
51. A. Dollfus, M. Wolff, J. E. Geake, *et al.*, in R. P. Binzel, T. Gehrels, and M. S. Matthews (Eds.), "Asteroids II," p. 594 (University of Arizona Press, Tucson, AZ, 1989).
52. P. Helfenstein, N. Currier, B. E. Clark, J. Veverka, M. Bell, *et al.*, Icarus **135**, 41 (1998).
53. V. P. Tishkovets. J. Quant. Spectrosc. Radiat. Transfer **72**, 123 (2002).
54. A. Z. Dolginov, Yu. N. Gnedin, and N. A. Silant'ev. "Propagation and Polarization of Radiation in Cosmic Media" (Gordon and Breach, Basel, 1995).
55. D. A. Varshalovich, A. N. Moskalev, and V. K. Khersonskii. "Quantum Theory of Angular Momentum" (World Scientific, Singapore, 1988).
56. V. P. Tishkovets, P. V. Litvinov, and M. V. Lyubchenko. J. Quant. Spectrosc. Radiat. Transfer **72**, 803 (2002).
57. S. J. Weidenschilling, C. R. Chapman, D. R. Davis, and R. Greenberg, in R. Greenberg, A. Brahic (Eds.), "Planetary Rings," p. 367 (University of Arizona Press, Tucson, AZ, 1984).